ROYAL SOCIETY
OF CHEMISTRY

PAPER

Check for updates

View Article Online
View Journal | View Issue

Second-order Jahn–Teller effect induced high-temperature ferroelectricity in two-dimensional NbO₂X (X = I, Br)†

Huasheng Sun, Kaiming Deng, Erjun Kan [ID] * and Yongping Du [ID] *

Based on the first-principles calculations, we investigated the ferroelectric properties of two-dimensional (2D) materials NbO₂X (X = I, Br). Our cleavage energy analysis shows that exfoliating one NbO₂I monolayer from its existing bulk counterpart is feasible. The phonon spectrum and molecular dynamics simulations confirm the dynamic and thermal stability of the monolayer structures for both NbO₂I and NbO₂Br. Total energy calculations show that the ferroelectric phase is the ground state for both materials, with the calculated in-plane ferroelectric polarizations being 384.5 pC m⁻¹ and 375.2 pC m⁻¹ for monolayers NbO₂I and NbO₂Br, respectively. Moreover, the intrinsic Curie temperature T_C of monolayer NbO₂I (NbO₂Br) is as high as 1700 K (1500 K) from Monte Carlo simulation. Furthermore, with the orbital selective external potential method, the origin of ferroelectricity in NbO₂X is revealed as the second-order Jahn–Teller effect. Our findings suggest that monolayers NbO₂I and NbO₂Br are promising candidate materials for practical ferroelectric applications.

Introduction

Ferroelectric (FE) materials, which exhibit spontaneous polarization that can be switched by an external electric field, have attracted tremendous research interest over the past decades due to their wide applications in capacitors, sensors, and non-volatile memories.[1–4] In the literature, many efforts have been made to develop perovskite-type oxides, such as BaTiO₃, PbTiO₃, PbZr₁₋ₓTiₓO₃, and La₁/₃NbO₃ in which the cations have an electron configuration of d⁰ (Ti⁴⁺, Zr⁴⁺, Nb⁵⁺).[5–8] Moreover, the spontaneous polarization of these compounds is usually induced by off-centering of cations which originates from the second-order Jahn–Teller (SOJT) effect.[9,10] SOJT-active cations have been shown to induce structural distortion, which would break the inversion symmetry, by anisotropic covalent bonding with ligands. Interestingly, the Curie temperature T_c of these compounds is far above room temperature (*i.e.*, the T_c of BaTiO₃, PbTiO₃, PbZr₁₋ₓTiₓO₃, and La₁/₃NbO₃ is 393, 763, 659, and 473 K respectively).[11–14] This inspires us to search for high-temperature ferroelectric materials with SOJT-activated cations.

On the other hand, the urgent requirement for the miniaturization of electronic devices stimulates researchers to devote significant effort to reducing the thickness of thin-film

MIIT Key Laboratory of Semiconductor Microstructure and Quantum Sensing, and Department of Applied Physics, Nanjing University of Science and Technology, Nanjing 210094, People's Republic of China. E-mail: njustdyp@njust.edu.cn; ekan@ njust.edu.cn

† Electronic supplementary information (ESI) available. See DOI: https://doi.org/10.1039/d3na00245d

ferroelectrics.[15,16] However, the depolarization field will destroy ferroelectricity at critical thicknesses for conventional ferroelectric compounds.[17] Recently, the discovery of ferroelectricity in monolayer or few-layer van der Waals (vdW) materials provides new opportunities for reducing the size of ferroelectric devices to atomic thickness.[18–22] In addition, the weak interlayer interaction and the dangling bond-free surface of two-dimensional (2D) vdW materials make it easy to integrate them with other materials in applications.

Thanks to the development of high-throughput calculations and machine learning methods, plenty of calculations have been proposed to predict promising 2D ferroelectric materials. However, only a few dozens of them have been confirmed by experiments.[13,14] The most intuitive strategy for designing new 2D ferroelectric materials is to use the structure of existing 2D ferroelectric materials in the databases as a prototype and then test different combinations of chemical elements. To date, only tens of prototypes, like CuInP₂S₆ type,[15,16] SnTe type,[17,18] α-In₂Se₃ type,[19,20] 1T′-MoTe₂ type,[21,22] sliding ferroelectrics and so on, are proposed theoretically and experimentally. Another strategy is to design new prototypes of 2D ferroelectric structures. Investigating the cation off-centring induced by the SOJT effect may provide insight into the design of new 2D ferroelectric structure prototypes.

In this work, we propose a new 2D ferroelectric structure prototype whose structural distortion is induced by the SOJT effect. Using first-principles calculations, we comprehensively investigate the ferroelectric properties of monolayer NbO₂I cleaved from its existing bulk counterpart. Total energy calculations show that the ferroelectric phase is the ground state with

an in-plane ferroelectric polarization of 384.5 pC m^{-1}, and the intrinsic Curie temperature T_c as high as 1700 K. Moreover, with the orbital selective external potential (OSEP) method,[23] we reveal that the SOJT effect originates ferroelectricity in NbO_2I. The finite indirect band gap is about 0.95 eV, which indicates that monolayer NbO_2I is a semiconductor. The carrier mobilities of electrons and holes along the two directions are different due to the crystal anisotropy. We also systematically studied the electronic and ferroelectric properties of monolayer NbO_2Br, which has the same structure as NbO_2I with the replacement of I atoms by Br atoms. Our numerical results show that the properties of NbO_2Br are very similar to the ones of NbO_2I.

Calculation methods

All calculations in this work were based on density functional theory (DFT) implemented in the Vienna *Ab initio* simulation package (VASP).[24] The generalized gradient approximation (GGA) with the form proposed by Perdew, Burke, and Ernzerhof (PBE)[25] was chosen as the exchange–correlation functional. The Projector Augmented Wave (PAW) method[26] was used to describe electron–ion interactions. The vacuum distance was set larger than 30 Å in order to avoid spurious periodic interactions. The kinetic energy cutoff was set to 550 eV, and the first Brillouin zone was sampled with a grid of $17 \times 15 \times 1$ k points according to the Monkhorst–Pack scheme.[27] The convergence criteria for electronic and ionic relaxations are 10^{-6} eV per atom and 10^{-3} eV Å^{-1}, respectively. van der Waals (vdW) correction was included using the D2 method.[28] The electronic contribution to polarization was calculated using the Berry phase method.[29,30] The nudged elastic band (NEB) approach[31,32] was used to simulate the minimum energy path (MEP) and associated energy barriers.

Results and discussion

The bulk NbO_2I material was successfully synthesized experimentally in 2007.[33] The crystal structure of NbO_2I possesses a centrosymmetric space group *Pnma* with a 7-coordinated Nb^{5+} cation and is shown as an example in Fig. 1. Interestingly, 7 ligands of Nb^{5+} form a pentagonal bipyramid that is connected *via* the apical O_1 atoms to chains and *via* three O_2 atoms to the double-layer structure (Fig. 1(b)). Between these double layers there are only weak van der Waals interactions of I atoms. Two I atoms and three O_2 atoms are on the pentagonal base plane. At the same time, the axial sites are occupied by the O_1 atom with very different Nb–O_1 distances of 1.78 and 2.20 Å, which indicate the shift of Nb^{5+} and form the structural distortion which could cause the polarization denoted in Fig. 1(c). However, the other Nb^{5+} ion in the double layer shifts to the opposite direction (Fig. 1(a)), and thus the bulk NbO_2I does not exhibit macroscopic polarization. As a comparison, the compound UO_2Br has a crystal structure very similar to NbO_2I except for equal U–O_1 distances and no displacement of the U atom (for details see Fig. S1†).[34] Thus, the space group of UO_2Br is *Cmcm* with inversion symmetry and has only the paraelectric (PE) phase without spontaneous polarization.
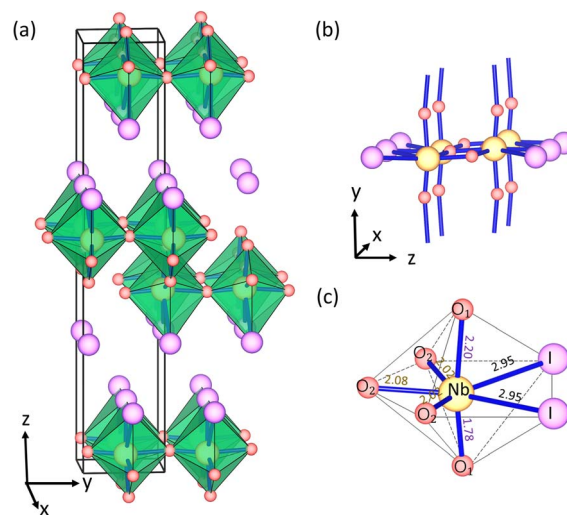

Fig. 1 (a) The layered bulk crystal structure of NbO_2I. (b) The connectivity of the polyhedral in NbO_2I. (c) Coordination polyhedron and bond length of Nb^{5+} in NbO_2I.

Because the bulk NbO_2I has a layered structure, it is of much interest to investigate the NbO_2I monolayer for promising ferroelectricity and other valuable properties. We first calculate the cleavage energy to check the accessibility of exfoliation and show the results in Fig. 2(a). The cleavage energy for NbO_2I and NbO_2Br is 0.28 and 0.21 J m^{-2}, respectively. They are smaller than the one of graphite.[35] The smaller cleavage energy means that the exfoliation of NbO_2I and NbO_2Br is feasible. Thus, one layer NbO_2I and NbO_2Br can be exfoliated from their bulk counterparts, as shown in the inset of Fig. 2.

The crystal structure dynamics and thermal stability can be explored by calculating the phonon spectra and molecular dynamics (MD) simulations. The phonon spectra of NbO_2I and NbO_2Br along the high-symmetry lines are plotted in Fig. 4(a) and (b). It is observed that there is no imaginary phonon frequency in the entire Brillouin zone, confirming that NbO_2I and NbO_2Br are dynamically stable. Considering the probability of successful experimental fabrication, the MD simulation of a 5
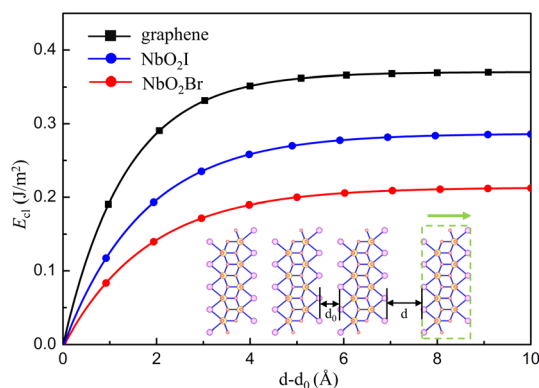

Fig. 2 Cleavage energy E_{cl} *versus* the separation distance $d-d_0$ in the process of exfoliating one NbO_2X (X = I, Br) layer from their bulk counterparts illustrated by the inset.

× 5 supercell at 500 K with 5 ps time is carried out. The results are presented in Fig. 4(c) and (d) for NbO_2I and NbO_2Br, respectively. The MD simulation suggests the thermal stability of the two monolayers. For monolayer NbO_2Br, we systematically search all possible 2D structures with the Nb : O : Br composition equal to 1 : 2 : 1 using the particle swarm optimization (PSO)[36] structure search algorithm and first-principles calculations. After comprehensive calculation, we found that there are six most energetically stable structures, as listed in Fig. S2.† However, the most stable structure is still our NbO_2I

Fig. 3 (a) Relative energy per unit cell (in meV) of monolayer NbO_2X (X = I and Br) at different polarization directions and takes the energy of FE as reference. (b) Schematic diagram of different polarization directions, where the direction of the arrow indicates the displacement direction of the Nb atom.

prototype structure, which again confirms that our NbO_2I monolayer prototype is stable.

Now we start to explore the ferroelectric properties of monolayers NbO_2I and NbO_2Br. As we analyzed before, Nb^{5+} has a displacement from the centre of pentagonal bipyramids, causing the spontaneous polarization. To find the ground state, we set three configurations of Nb^{5+} in the monolayer, namely ferroelectric (FE), paraelectric (PE), and antiferroelectric (AFE), as shown by the schematics in Fig. 3(b). The total energies of the three configurations are illustrated in Fig. 3(a), in which we use the energy of FE as a reference energy and set it to zero. We can easily see that the FE state is the ground state, which is totally different from bulk NbO_2I with two Nb^{5+} ions in one layer shifting in opposite directions.

The fully relaxed monolayer structure reveals that the Nb^{5+} ion shifts from the centre of pentagonal bipyramids with an unequal bond length with two apical O_1 atoms. The polarization is therefore in the in-plane direction. By using the Berry phase method, the polarization Ps was estimated, with values equal to 384.5 and 375.2 pC m^{-1} for NbO_2I and NbO_2Br, respectively. The reversal of polarization is realized through a phase transition between two symmetry-equivalent ferroelectric states with opposite Ps. We constructed two potential switching paths and computed the energy evolution using the NEB approach as shown in Fig. 5(a) and (b) in order to explore the polarization switching and the pertinent energy barrier of 2D NbO_2I and NbO_2Br. The PE phase is the intermediate state of the first path,
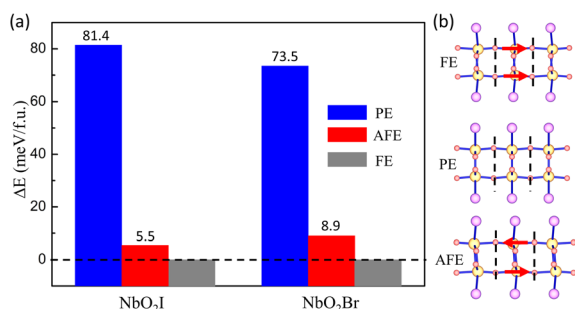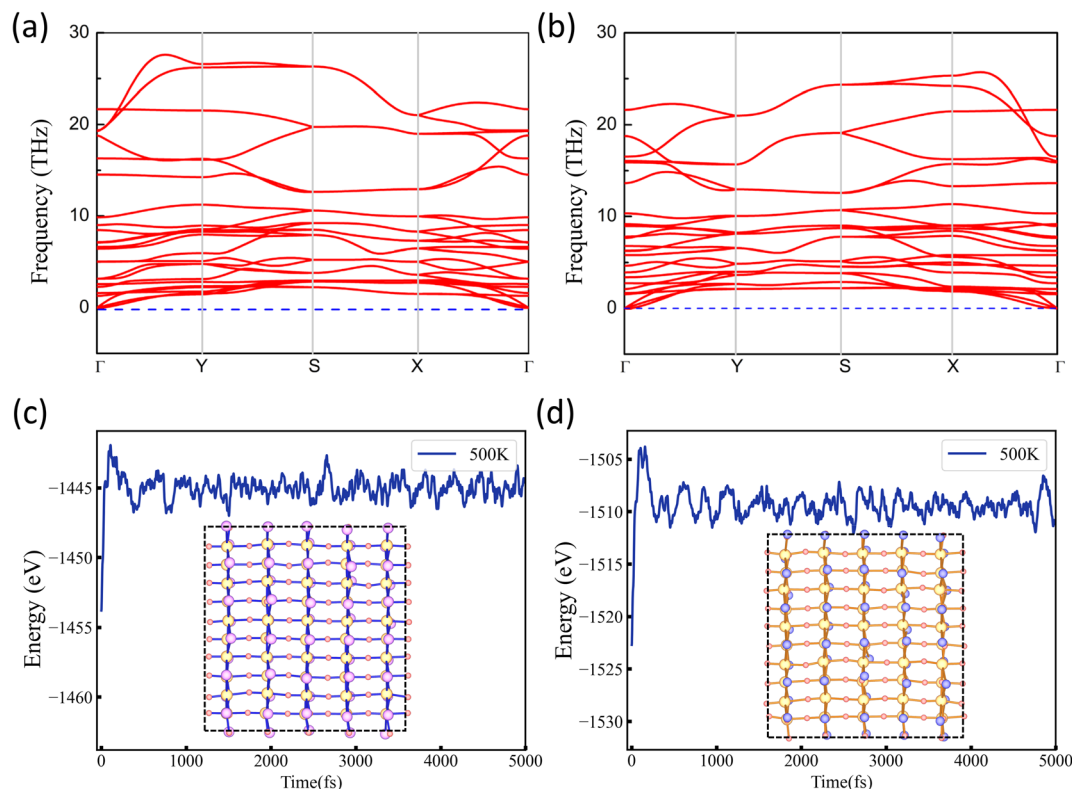

Fig. 4 (a) and (b) Phonon dispersions of the NbO_2X (X = I and Br) monolayer. (c) and (d) Evolution of total energy for the NbO_2I and NbO_2Br monolayers at 500 K from molecular dynamics simulation. Insets present the snapshots at the end of simulations.
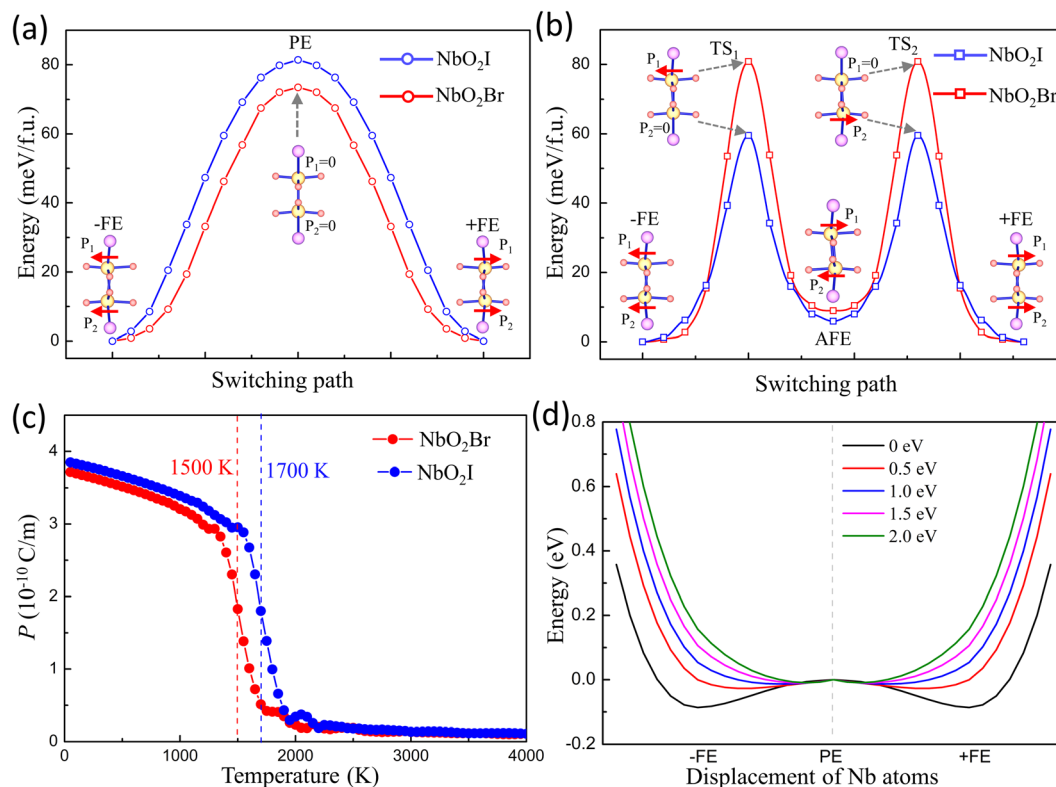
Fig. 5 The energy evolution of two polarization switching paths of the FE NbO$_2$X monolayer in two cases: (a) the transition proceeds through an intermediate PE phase; (b) the intermediate phase during the switching path is the AFE configuration. The inset views display the structures of initial, transition (TS), and final states, where the direction of the red arrow indicates the displacement direction of the Nb atom. (c) Curie temperatures of NbO$_2$X monolayers using Monte Carlo (MC) simulations. (d) The double-well evolution as the external potential applied on Nb 4d$_{xy}$ and 4d$_{xz}$ orbitals.

and the AFE phase is the intermediate state of the second path. We discovered that the first path's energy barrier, which uses the PE phase as an intermediate state, is around 80 meV, whereas the second path's energy barrier is 60 meV. As a result, we came to the conclusion that the FE-AFE-FE transformation is possible during the NbO$_2$I monolayer's ferroelectric switching. However, in the case of the NbO$_2$Br monolayer, there is a slight difference (7 meV) of the energy barrier between the first and second paths. This indicates a potential transformation path of FE-PE-FE for the NbO$_2$Br monolayer that differs from the behaviour of the NbO$_2$I monolayer.

Ferroelectricity is further emphasized by the Curie temperature above which the macroscopic spontaneous polarization disappears. The effective Hamiltonian of NbO$_2$I and NbO$_2$Br supercells is carried out by applying the Landau–Ginzburg phase transition theory (for more details see ESI†). After fitting the parameters of effective Hamiltonian we perform the Monte Carlo simulation to investigate the T_c of 2D NbO$_2$I and NbO$_2$Br. The numerical results are shown in Fig. 5(c), and the T_c of the NbO$_2$I (NbO$_2$Br) monolayer is as high as 1500 K (1700 K) that again proves that NbO$_2$X is a stable and robust 2D ferroelectric material.

It is well known that in the local coordinate of a pentagonal bipyramid, the d orbitals will be split into three groups by the crystal field. The d$_{xz}$ and d$_{yz}$ orbitals possess the lowest energy.

When we transfer to the global coordinate of NbO$_2$I, the local d$_{xz}$ and d$_{yz}$ of Nb^{5+} in the pentagonal bipyramid will transfer to d$_{xy}$ and d$_{xz}$. In the following parts, we will discuss the results in the global coordinate. The critical mechanism and feature of the SOJT effect are the hybridization between the empty cation's d orbitals (i.e., Ti^{4+}, Nb^{5+}) and occupied anion's p orbitals (i.e., O^{2-}, I^{1-}).[37] Moreover, Wheeler and Hoffman et al.[38] and Kunz and Brown[39] pointed out that the magnitude of the distortion of the cation surrounded by its ligands (i.e., TiO$_6^{2-}$, NbO$_5$I$_2$ pentagonal bipyramid in this work) attributable to the SOJT effect depends on the strength of hybridization between the empty cation's d orbitals and occupied anion's 2p orbitals.

The density of states of NbO$_2$I is plotted in Fig. 6(c). The partial density of states (PDOS) clearly shows that both apical O$_1$-2p and planar O$_2$-2p orbitals are mainly located between −8 and −1 eV, indicating that the 2p orbitals of apical O$_1$ and planar O$_2$ are fully occupied. The I-5p orbitals are mainly distributed from −5 eV to Fermi energy with a narrower bandwidth. The Nb-4d orbitals are located above the Fermi energy with the 4d^0 configuration. However, there are finite states of 2p$_y$ and 2p$_z$ of apical O$_1$ distributing between 0.5 and 3 eV, where there are also major contributions from Nb 4d$_{xy}$ and 4d$_{xz}$, which means that there are strong hybridizations between unoccupied Nb 4d$_{xy}$ and 4d$_{xz}$ orbitals and occupied apical O$_1$ 2p$_y$ and 2p$_z$, indicating the SOJT effect in NbO$_2$I. The electronic
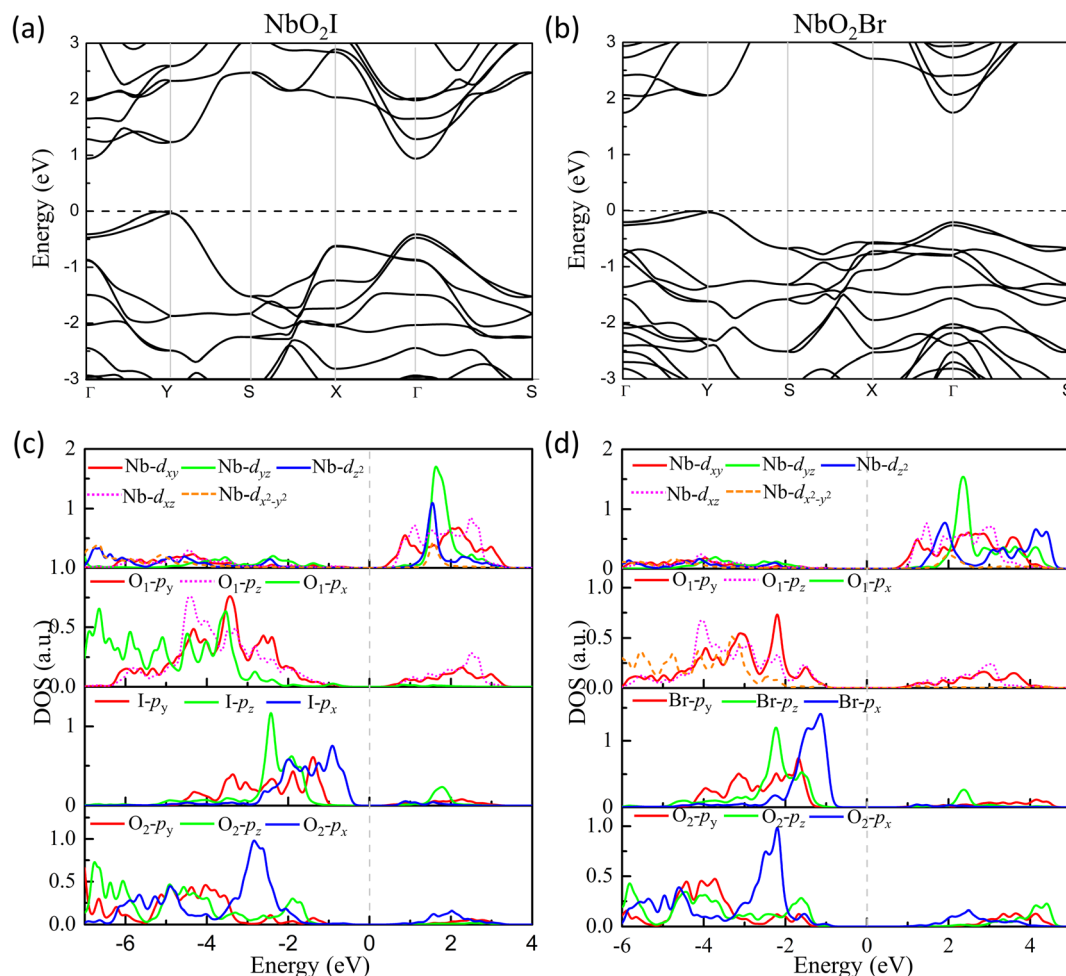
Fig. 6 Energy band structures (a) and (b) for FE NbO$_2$X monolayers. Projected density of states (PDOS) for monolayers (c) NbO$_2$I and (d) NbO$_2$Br.

structure of NbO$_2$Br shown in Fig. 6(d) is very similar to that of NbO$_2$I. As a result, we will not give a detailed discussion about NbO$_2$Br.

According to our discussion above, if we tune the strength of the hybridization, we can adjust the SOJT effect and further investigate the FE phase transition. Here, we apply the OSEP method by adding an external potential to raise the energy of Nb-4d$_{xy}$ and 4d$_{xz}$ orbitals by different values to increase the energy difference between them and O$_1$ 2p$_y$ and 2p$_z$. The OSEP approach can introduce an exceptional external potential that only can be felled by certain appointed orbitals.[23] We take the 2 eV potential on Nb-4d$_{xy}$ and 4d$_{xz}$ as an example shown in Fig. S7.† The DOS of Nb-4d$_{xy}$ and 4d$_{xz}$ is indeed shifted-up by almost 2 eV, which indicates that the OSEP approach can effectively shift the energy of certain selective orbitals. More interestingly, due to a larger energy difference between Nb 4d$_{xy}$/4d$_{xz}$ and O$_1$ 2p$_y$/2p$_z$, the strength of hybridization between them is decreased. One can expect that the SOJT effect induced distortion will disappear and result in a PE ground state instead of FE when hybridization between them vanishes.

Thus, we apply different external potentials on Nb-4d$_{xy}$ and 4d$_{xz}$ to study the FE phase transition in NbO$_2$I. Fig. 5(d) illustrates the results. When the external potential on Nb-4d$_{xy}$ and

4d$_{xz}$ rises, the characteristic double well of monolayer NbO$_2$I becomes shallower and eventually disappears, suggesting that the ground state becomes the PE phase. The same calculation is also carried out for NbO$_2$Br, and the same behaviour of double well evolution is obtained (shown in Fig. S6†). These results demonstrate that the SOJT effect is the reason for the ferroelectric phase transition.

Regarding the ferroelectricity, the band structure of NbO$_2$X monolayers is also calculated. Our numerical results demonstrate that both monolayers NbO$_2$I and NbO$_2$Br are Indirect bandgap semiconductors with $E_g = 0.95$ eV and 1.75 eV, respectively. As illustrated in Fig. 4, their valence band maximum (VBM) is near the Y point, while their conduction band minimum (CBM) is at the Γ point. The effective mass at the VBM for NbO$_2$I is 0.48 m0 along the x axis and 1.37 m_0 along the y axis, and the effective mass at the CBM is 0.44 m_0 along the x axis and 1.18 m_0 along the y axis, where m_0 is the electron mass (for more details see ESI†). Different effective mass values along the two axes show band structure anisotropy, which is caused by crystal structure anisotropy. Interestingly, the carrier mobility of holes is an order of magnitude greater than that of electrons, implying that NbO$_2$I is an excellent P-type semiconductor.

Conclusions

In summary, we explored the crystal structure, ferroelectric, and electronic properties of monolayers NbO_2I and NbO_2Br using first-principles calculation. We clarified that the FE phase is the energetically stable phase. The origin of polarization comes from the displacement of Nb^{5+} cations driven by the SOJT effect. The monolayers NbO_2I and NbO_2Br are indirect semiconductors with the calculated band gap of 0.95 eV and 1.75 eV respectively. In addition, the carrier mobility shows anisotropy along two directions. Our findings add a new member to the family of 2D ferroelectric prototypes, providing a microscopic mechanism of the FE phase transition that will help the discovery and design of new FE materials.

Conflicts of interest

There are no conflicts to declare.

Acknowledgements

References

1 C. Wang, Y. Lu, D. Cobden and J. Wang, *Nat. Mater.*, 2023, **22**, 542–552.

2 L. Qi, S. Ruan and Y.-J. Zeng, *Adv. Mater.*, 2021, **33**, 2005098.

3 X.-K. Wei, N. Domingo, Y. Sun, N. Balke, R. E. Dunin-Borkowski and J. Mayer, *Adv. Energy Mater.*, 2022, **12**, 2201199.

4 Z. Guan, H. Hu, X. Shen, P. Xiang, N. Zhong, J. Chu and C. Duan, *Adv. Electron. Mater.*, 2020, **6**, 1900818.

5 D. Kepaptsoglou, J. D. Baran, F. Azough, D. Ekren, D. Srivastava, M. Molinari, S. C. Parker, Q. M. Ramasse and R. Freer, *Inorg. Chem.*, 2018, **57**, 45–55.

6 V. F. Michel, T. Esswein and N. A. Spaldin, *J. Mater. Chem. C*, 2021, **9**, 8640–8649.

7 J. Zhao, J. Gao, W. Li, Y. Qian, X. Shen, X. Wang, X. Shen, Z. Hu, C. Dong, Q. Huang, L. Cao, Z. Li, J. Zhang, C. Ren, L. Duan, Q. Liu, R. Yu, Y. Ren, S.-C. Weng, H.-J. Lin, C.-T. Chen, L.-H. Tjeng, Y. Long, Z. Deng, J. Zhu, X. Wang, H. Weng, R. Yu, M. Greenblatt and C. Jin, *Nat. Commun.*, 2021, **12**, 747.

8 R. Cervasio, Y. Peperstraete, T. Maroutian, R. Haumont, M. Verseils, J.-B. Brubach, R. Tétot, J. Creuze, P. Roy and E. Amzallag, *J. Phys. Chem. C*, 2022, **126**, 12860–12869.

9 A. S. Ivanov, K. V. Bozhenko and A. I. Boldyrev, *Inorg. Chem.*, 2012, **51**, 8868–8872.

10 I. B. Bersuker, *Chem. Rev.*, 2021, **121**, 1463–1512.

11 L. Gigli, M. Veit, M. Kotiuga, G. Pizzi, N. Marzari and M. Ceriotti, *npj Comput. Mater.*, 2022, **8**, 209.

12 G. Sághi-Szabó, R. E. Cohen and H. Krakauer, *Phys. Rev. Lett.*, 1998, **80**, 4321–4324.

13 H. Brunckova, L. Medvecky, A. Kovalcikova, M. Fides, E. Mudra, J. Durisin, M. Sebek, M. Kanuchova and J. Skvarla, *J. Rare Earths*, 2017, **35**, 1115–1125.

14 N. Zhang, H. Yokota, A. M. Glazer, Z. Ren, D. A. Keen, D. S. Keeble, P. A. Thomas and Z. G. Ye, *Nat. Commun.*, 2014, **5**, 5231.

15 G. R. Bhimanapati, Z. Lin, V. Meunier, Y. Jung, J. Cha, S. Das, D. Xiao, Y. Son, M. S. Strano, V. R. Cooper, L. Liang, S. G. Louie, E. Ringe, W. Zhou, S. S. Kim, R. R. Naik, B. G. Sumpter, H. Terrones, F. Xia, Y. Wang, J. Zhu, D. Akinwande, N. Alem, J. A. Schuller, R. E. Schaak, M. Terrones and J. A. Robinson, *ACS Nano*, 2015, **9**, 11509–11539.

16 L. W. Martin and A. M. Rappe, *Nat. Rev. Mater.*, 2016, **2**, 16087.

17 J. Junquera and P. Ghosez, *Nature*, 2003, **422**, 506–509.

18 R. Fei, W. Kang and L. Yang, *Phys. Rev. Lett.*, 2016, **117**, 097601.

19 C. Liu, R. Gao, X. Cheng, X. Yang, G. Qin, H. Gao, S. Picozzi and W. Ren, *Phys. Rev. B*, 2023, **107**, L121402.

20 H. Ai, X. Song, S. Qi, W. Li and M. Zhao, *Nanoscale*, 2019, **11**, 1103–1110.

21 C. Cui, F. Xue, W.-J. Hu and L.-J. Li, *npj 2D Mater. Appl.*, 2018, **2**, 18.

22 L. H. Jin, H. D. Wang, R. Cao, K. Khan, A. K. Tareen, S. Wageh, A. A. Al-Ghamdi, S. J. Li, D. B. Li, Y. Zhang and H. Zhang, *APL Mater.*, 2022, **10**, 060903.

23 (a) X. Wan, J. Zhou and J. Dong, *Europhys. Lett.*, 2010, **92**, 57007; (b) Y. Du, H.-C Ding, H.-C Sheng, S. Y. Savrasov, X. Wan, C.-G. Duan and J. Phys, *Condens. Matter*, 2013, **26**, 025503.

24 (a) Y. Du, H.-C. Ding, L. Sheng, S. Y. Savrasov, X. Wan and C.-G. Duan, *J. Phys.: Condens. Matter*, 2013, **26**, 025503; (b) G. Kresse and J. Furthmüller, *Comput. Mater. Sci.*, 1996, **6**, 15–50.

25 J. P. Perdew, K. Burke and M. Ernzerhof, *Phys. Rev. Lett.*, 1997, **78**, 1396.

26 G. Kresse and D. Joubert, *Phys. Rev. B: Condens. Matter Mater. Phys.*, 1999, **59**, 1758–1775.

27 H. J. Monkhorst and J. D. Pack, *Phys. Rev. B: Solid State*, 1976, **13**, 5188–5192.

28 S. Grimme, *J. Comput. Chem.*, 2006, **27**, 1787–1799.

29 R. D. King-Smith and D. Vanderbilt, *Phys. Rev. B: Condens. Matter Mater. Phys.*, 1993, **47**, 1651–1654.

30 R. Resta, *Rev. Mod. Phys.*, 1994, **66**, 899–915.

31 G. Henkelman, B. P. Uberuaga and H. Jonsson, *J. Chem. Phys.*, 2000, **113**, 9901–9904.

32 N. A. Zarkevich and D. D. Johnson, *J. Chem. Phys.*, 2015, **142**, 024106.

33 S. Hartwig and H. Hillebrecht, *Z Naturforsch B*, 2007, **62**, 1543–1548.

34 M.-J. Crawford, A. Ellern, K. Karaghiosoff, P. Mayer, H. Nöth and M. Suter, *Inorg. Chem.*, 2004, **43**, 7120–7126.

35 R. Zacharia, H. Ulbricht and T. Hertel, *Phys. Rev. B: Condens. Matter Mater. Phys.*, 2004, **69**, 155406.
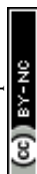
36 H. Wang, Y. Wang, J. Lv, Q. Li, L. Zhang and Y. Ma, *Comput. Mater. Sci.*, 2016, **112**, 406–415.

37 Y. Inaguma, A. Aimi, Y. Shirako, D. Sakurai, D. Mori, H. Kojitani, M. Akaogi and M. Nakayama, *J. Am. Chem. Soc.*, 2014, **136**, 2748–2756.

38 R. A. Wheeler, M. H. Whangbo, T. Hughbanks, R. Hoffmann, J. K. Burdett and T. A. Albright, *J. Am. Chem. Soc.*, 1986, **108**, 2222.

39 M. Kunz and I. D. Brown, *J. Solid State Chem.*, 1995, **115**, 395.